Natural Hazards (2024) 120:2749–2775
https://doi.org/10.1007/s11069-023-06303-4

ORIGINAL PAPER

Investigation of multi-annual groundwater response to rainfall in a deep-seated bedrock landslide: the case of the Kualiangzi landslide, China

Han-Xiang Liu[1,2] · Qiang Xu[1,2] · Tong Qiu[3] · Jiang Li[1]

Received: 11 September 2022 / Accepted: 27 October 2023 / Published online: 7 December 2023

Abstract
The hydrological response of groundwater to rainfall plays a key role in the initiation of deep-seated bedrock landslides; however, the mechanisms require further investigation due to the complexity of groundwater movement in fissured bedrock. In this study, an active translational landslide along nearly horizontal rock strata was investigated. The hydrological response of groundwater to rainfall was analyzed, using the data from a four-year real-time field monitoring program from June 2013 to December 2016. The monitoring system was installed along a longitudinal section of the landslide with severe deformation and consisted of two rainfall gauges, nine piezometers, three water-level gauges, and two GPS data loggers. Much research effort has been directed to exploring the relationship between rainfall and groundwater response. It is found that both the pore-water pressure (PWP) and groundwater level (GWL) responses were significantly influenced by the rainfall pattern and the hydrological properties of the underlying aquifer. The rapid rise and fall of PWP and GWL were observed in the rainy season of 2013 with high-frequency, long-duration, and high-intensity rainfall patterns, especially in the lower section of the landslide dominated by the porous aquifer system. In contrast, a slower and prolonged response of PWP and GWL to rainfall was observed in most monitoring boreholes in 2014 and 2015 with two rainstorms of short duration and high intensity. In the lower section of the landslide, the peak GWL exhibited a stronger correlation with the cumulative rainfall than the daily rainfall in a single rainfall event whereas the peak groundwater level fluctuation (GWLF) exhibited a strong correlation with API with a half-life of 7 days. In the middle section of the landslide, however, relatively lower correlation between rainfall and groundwater response was observed. Three types of groundwater flow were identified based on the recession coefficients of different segments of water-level hydrographs in the landslide area, corresponding to the quick flow through highly permeable gravely soil and well-developed vertical joints in the bedrock, the slow and diffuse flow through the relatively less-permeable bedrock, and the transition between them in the aquifer system.

Keywords Deep-seated landslide · Groundwater level · Hydrograph · Pore-water pressure · Rainfall pattern · Slope displacement

Extended author information available on the last page of the article

1 Introduction

In tropical and subtropical regions, the vast majority of landslides are related to seasonal rainfall episodes. Numerous studies have attempted to explore the correlation between rainfall and landslide occurrence (Glade et al. 2000; Ruette et al. 2011; Ran et al. 2018). Different thresholds, such as rainfall, soil moisture, and hydrological conditions, have been proposed for the predication and early warning of landslides (Crozier 1999; Crosta and Frattini 2003; Jakob and Weatherly 2003). The most commonly used rainfall threshold is the ID model, which combines rainfall intensity and duration (Caine 1980; Guzzetti et al. 2008; Postance et al. 2018). However, these empirical (statistical) methods lack theoretical framework for understanding how the hydrogeological responses of groundwater influence the location, timing, and rates of landslide movement. For a deep-seated rockslide, it is difficult to identify a rainfall threshold due to the complexity of hydrological process of groundwater in fissured rocks, which could cause a time lag of landslide occurrence from weeks to months (Uchida et al. 2003; Jitousono et al. 2008). Therefore, it is important to study the groundwater response to rainfall and its causative effect on slope instability, for a better understanding of the formation mechanism or quantitative predication and early warning of deep-seated landslides.

Some theoretical hydrological models have been developed to simulate the water infiltration process and to predict the groundwater level in an aquifer (Sangrey et al. 1984; Van Asch et al. 1996; Iverson 2000). The calculated groundwater levels can be used as an input to a stability model to evaluate the temporal instability of a landslide (Van Asch and Buma 1997; Hong and Wan 2011; Li et al. 2016). Using theoretical methods, however, it is challenging to: (1) obtain certain physical parameters of soil/rock required by theoretical models for complex landslides, and (2) account for three-dimensional landslide geometries and geological heterogeneities. Alternatively, field monitoring has been used to effectively study the groundwater fluctuation in relation to rainfall. Many studies reported the monitoring results on soil and shallow landslides (e.g., Ogawa et al. 1987; Iverson and Major 1987; Gabet et al. 2004; Matsuura et al. 2008; Saito et al. 2010). However, for a deep-seated rockslide, groundwater flow in a bedrock fissure network always causes complex groundwater movement, and the mechanisms of groundwater in initiating a deep-seated rockslide are still unclear.

Relationships between rainfall, groundwater, and slope movement of rainfall-triggered deep-seated landslides have been studied by many researchers (Zhang et al. 2006; Matsuura et al. 2008; Chigira 2009; Tsou et al. 2011; Prokešová et al. 2013; Vallet et al. 2016). Van Asch et al. (1996) simulated the groundwater response to rainfall in a landslide consisting of varved clays and measured the horizontal infiltrate rates from fissures into the surrounding silt layers in varved clays. They revealed that water storage in the colluvial cover played a crucial role in water level and residence time in the fissures of the underlying varved clays, and the landslide could be caused by the hydrostatic pressure in the fissure system before a complete saturation of the varved clays. For deep-seated landslides in rock strata, Hong et al. (2005) employed a tank model to simulate the groundwater variations in a crystalline schist landslide, which permitted the change of water levels in future rainfall events to be predicted and rainfall-induced landslide movement to be estimated. Padilla et al. (2014) concluded that the surficial soil and the underlying bedrock were two separate hydrological systems based on observation data from a 10-m borehole (surficial aquifer) and a 40-m borehole (bedrock aquifer) of a hillslope. A unique fractured structure, which was caused by the gravitational deformation of the slope, rapidly drove the rainfall water through the bedrock, strongly influenced the slope

stability, and was responsible for the initiation of a deep-seated landslide during high-precipitation events. Due to site-specific characteristics of rock, it is challenging to obtain causal relationships between rainfall and rockslides in light of the difficulties behind theoretical models and limited field measurements of rock slide cases. In recent years, machine learning methods have been gradually used in exploring those relationships for large and complex landslides (Krkač et al. 2017; Wei et al. 2019); however, an incomplete understanding of hydrogeological process of groundwater in the slope creates challenges in the interpretability of the identified relationships.

In this paper, the Kualiangzi landslide, which is a typical deep-seated bedrock landslide, occurred in the nearly horizontal rock strata of Sichuan Basin, China, is studied. The bedrock consists of alternating thick sandstone and thin mudstone layers (Huang et al. 2005). Differential deformations among these alternating layers have caused a number of vertical tension cracks or troughs in the slope. Based on the geomechanical model developed by Zhang et al. (1994), the initiation of the Kualiangzi landslide was mainly caused by the rising hydrostatic pressure in the vertical cracks at the rear edge of the slope and the rising uplift pressure along the bottom slip surface during rainstorms (Ji et al. 2000; Xu et al. 2016). The reduction in shear strength due to the softening of mudstone/clayey soil on the slip surface was also responsible for the creep movement of the landslide in the dry season (Chen 2014). In order to study the groundwater response to rainfall and its impact on the slope stability, field monitoring of rainfall, groundwater, and surficial displacement has been carried out since 2013. Based on data collected in the rainy season of 2013, Xu et al. (2016) observed a pronounced increase in groundwater level and pore-water pressure after a rainstorm, with a time lag between the start of increase and the onset of the rainstorm. The water level in the tension trough at the rear edge of the landslide had a high negative correlation with the slope stability factor and was suggested as one of the early-warning indicators.

The main purpose of this study is to explore the seasonal and annual variations of groundwater to rainfall of the Kualiangzi landslide based on the field measurements during a four-year period between 2013 and 2016. Different rainfall parameters (i.e., daily rainfall, cumulative rainfall, and antecedent precipitation index), groundwater response parameters (i.e., pore-water pressure, groundwater level, and their fluctuations), and displacement parameters at the landslide surface (i.e., cumulative displacement and displacement rate) were utilized to study the relationships between rainfall, groundwater response, and slope movement. In the following sections, the landslide site and field instrumentation are first briefly described as detailed description can be found in Xu et al. (2016). The field monitoring results are subsequently presented and discussed with a focus on the temporal and spatial groundwater response to heavy rainfalls. Finally, the groundwater flow characteristics based on hydrograph analyses are discussed. It should be noted that this study extended the scope of Xu et al. (2016) which only focused on the flood season in 2013. The relationship of landslide displacement with water pressure is not the focus of this paper due to the lack of sufficient data to quantify such relationship during the four-year period.

2 Landslide case and field monitoring program

2.1 Overview of landslide case

The Kualiangzi landslide area is located in Zhongjiang County, Deyang City, Sichuan Province as shown in Fig. 1. The landslide body is 1100 m wide, 360–390 m long, and

30–80 m thick, forming a total volume of 2.55×10^7 m^3. The slope is gentle in the front of the landslide with an average gradient smaller than 5° and relatively steep in the back with a gradient of 25–35°. The landslide mass was divided into three zones mainly according to the severity of deformation and topographic features in each zone (Fig. 1). Zone I has the largest deformation with several large tension troughs at the rear edge and local collapses along the front and lateral boundaries of the landslide (Fig. 2). Trough-I (Figs. 2 and 3a) was caused by a large-scale slide in the rainy season of 1949 and formed its present width with a maximum of 60 m and length of about 1 km after the second large-scale slide in 1981. Trough-II (Figs. 2 and 3a) was caused by the intermittent landslide movements between 1950 and 1960s. The landslide movement still continues and is characterized by a relatively fast movement in the rainy season and a creep movement in the dry season annually. Figure 3b and c shows significant soil settlement and crack deformation in the cement piers of two water-level gauges just after the rainy season of 2015, which were installed in the middle section of the landslide in 2013. The piers of the monitoring gauges at the leading edge of the landslide were damaged. Several installed gauges malfunctioned due to damages of the monitoring boreholes or the transmission cables from the accumulated deformation.

The surficial layer of the landslide consists of gravelly soils with an average thickness of 10 m, whereas the underlying bedrock is composed of thick layers of sandstones interbedded by thin layers of mudstones with a dipping angle of 2°–5° (Fig. 4). The sandstones exhibited moderate to low weathering and had two sets of nearly vertical joints (Fig. 4) caused by differential deformations between sandstone and mudstone. Those joints provided channels for rainwater to infiltrate into the deep zone, causing the softening of mudstone and the formation of slip zone. Colluviums consisting of a mixture of rock blocks, gravels, and breccias cumulated in the tension troughs at the rear edge of the landslide. Calcification membrane was found on some rock blocks, indicating a strong groundwater movement in the troughs.

2.2 Hydrological background

The landslide area has a humid subtropical monsoon climate with an average annual precipitation of 844.5 mm. The infiltrated rainwater provides the main groundwater recharge in the landslide area. The groundwater flow field in the slope can be regarded

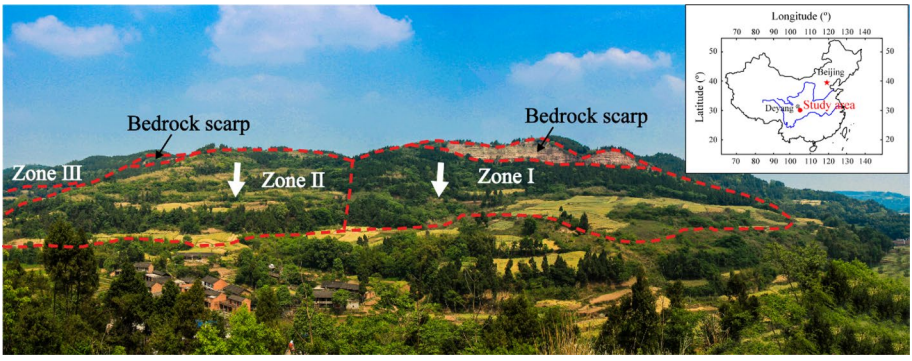

Fig. 1 A closed-up view of the Kualiangzi landslide (facing the east on an opposite hillslope of the landslide, photograph taken in 2015)

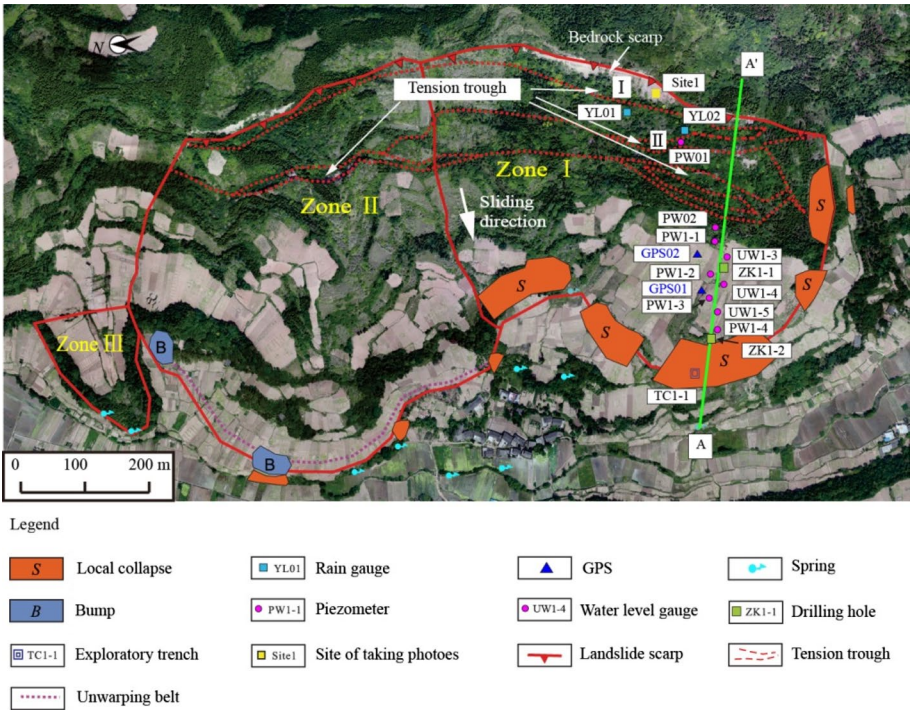

Fig. 2 Aerial view of the Kualiangzi landslide in 2013 and the layout of field monitoring system (revised from Xu et al. 2016)

as a separate hydrogeological unit. Two types of aquifer systems exist: a porous aquifer system consisting of the covering soil and a fissure aquifer system consisting of the alternating bedrock of sandstone and mudstone. The complex fissure/crack network in the shallow bedrock, including weathered fissures, tectonic fissures, and bedding planes, provides a storage space and transport pathways for groundwater, causing different groundwater responses to rainfall in these two aquifer systems. The previously formed tension troughs at the rear edge constitute the main water storage zone (Fig. 5a). During rainfall, driven by the water head difference, groundwater is discharged into the gully at the leading edge of the landslide in the forms of spring water (Fig. 5b) and channel drainage (Fig. 5c) along the transport pathways. In addition, the underlying intact bedrock serves as a relative water-resistant layer, above which an active zone of groundwater movement is formed. The thin mudstone intercalation in the zone is continuously softened by water, forming the slip zone of the landslide.

Lv et al. (2019) used multi-tracer tests, injection tests and electrical resistivity tomography to investigate the groundwater flow characteristics in the middle section of the Kualiangzi landslide. They concluded two modes of groundwater flow. One is the preferential flow which was controlled by the nearly vertical cracks of the bedrock and had the flow direction approximately perpendicular to the sliding direction. The other is the diffuse flow along the bedding planes of sandstone and mudstone, which showed a much smaller flow velocity than the preferential flow.

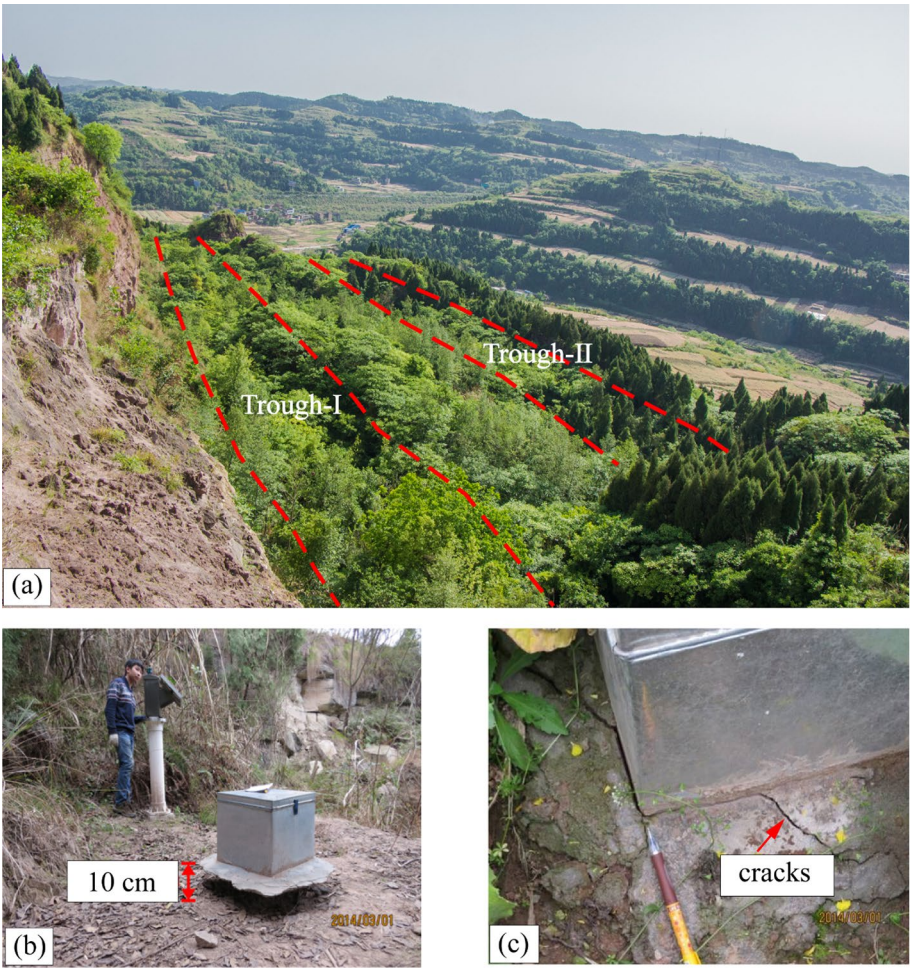

Fig. 3 Historical movements of the Kualiangzi landslide: **a** two large tension troughs at the rear edge (facing SW20° at the top of Trough-I); **b** soil settlement observed in the cement pier of a water-level gauge in the middle section of landslide; and **c** cracking deformation observed in the cement pier of a water-level gauge in the middle section of landslide

2.3 Monitoring system

Rainfall, groundwater level, pore-water pressure and the surficial slope displacement were monitored in real-time automatically. All sensors were installed near the longitudinal profile A-A' of Zone I in Fig. 2. The cross-sectional profile of A-A' and the installed sensors are shown in Fig. 6.

Nine piezometers were employed to monitor pore-water pressure and distributed in six boreholes named as PW01, PW02, PW1-1, PW1-2, PW1-3, and PW1-4 (see Fig. 6). There were two piezometers embedded at different depths in each of PW1-1, PW1-2, and PW1-3, named as PW1-1-1, PW1-1-2, PW1-2-1, PW1-2-2, PW1-3-1, and PW1-3-2, whereas only one piezometer was embedded in each of the other boreholes (i.e., PW01, PW02, and PW1-4). The main installation process of those piezometers is as

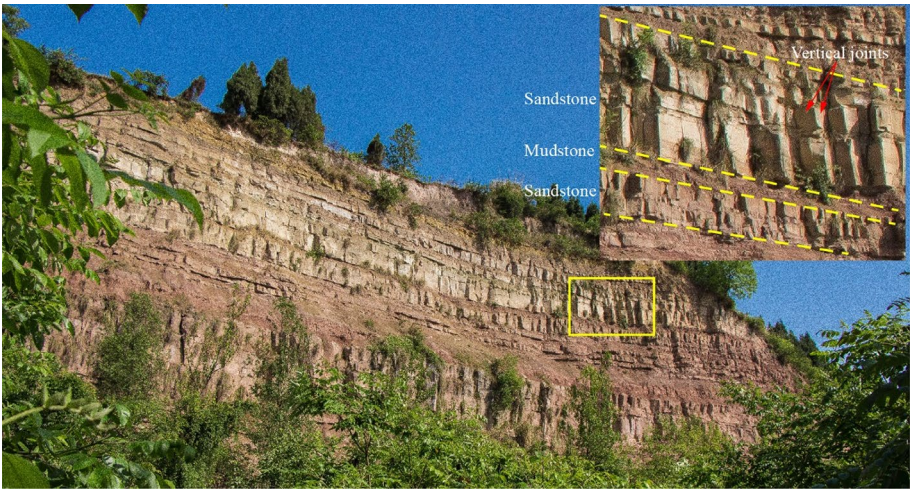

Fig. 4 Alternating beds of thick sandstone and thin mudstone exposed in the scarp of tension trough-I formed at the rear edge of the Kualiangzi landslide (see Site1 location in Fig. 2)

Fig. 5 Recharge and drainage of groundwater in the Kualiangzi landslide: **a** rainwater storage in the tension trough at the rear edge; **b** spring drainage at the leading edge; and **c** channel drainage at the leading edge

follows: after a piezometer was positioned at the desired depth, the hole was backfilled with sand of 20 cm in thickness and then with a mixture of bentonite and cement slurry up to the ground surface. If there were two piezometers positioned in a hole, the sand and bentonite should be alternatively backfilled to the lower part of the upper piezometer. Three water-level gauges were used to monitor groundwater level and installed in three boreholes numbered as UW1-3, UW1-4, and UW1-5 (see Fig. 6). These boreholes had the lateral drainage pipes equipped with strainers. In addition, two rain gauges (i.e., Y01 and Y02) and two displacement monitoring stations (i.e., GPS01 and GPS02) were installed to monitor rainfall and surficial displacement, respectively.

To avoid repetition, a detailed description of the monitoring system is not included in this paper but can be found in Xu et al. (2016). Except for few water-level gauges (UW1-3, UW1-4, UW1-5) and piezometers (PW1-1-1, PW1-2-1, PW1-3-2), most sensors failed to record data continuously and reliably after 2016. Thus, our subsequent analyses will be based on the data recorded over a four-year span from 2013 to 2016. Table 1 lists the type, installation, and operating condition of all sensors from the date of installation to December 2016.

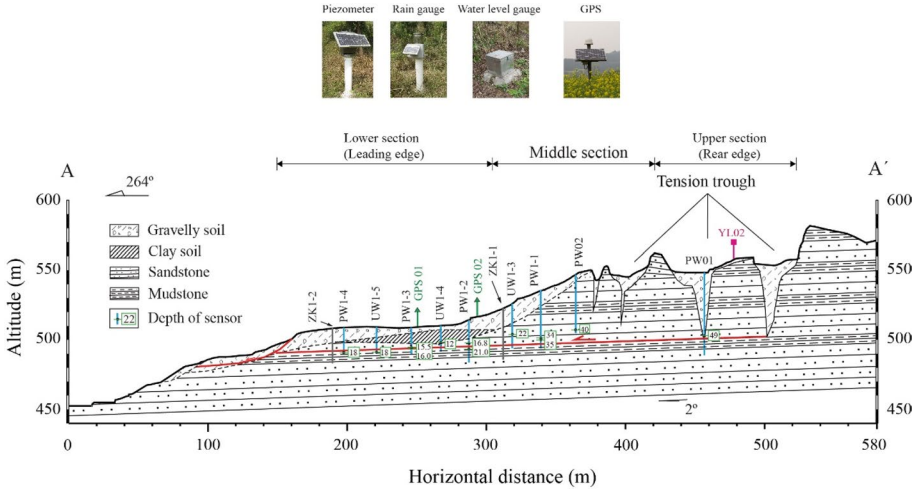

Fig. 6 Geological profile and layout of monitoring locations of section A-A′ in Fig. 2 (revised from Xu et al. 2016)

3 Results

3.1 Rainfall characteristics

The rainfall monitoring results from June 2013 to December 2016 are analyzed. Figure 7 shows the daily rainfall and cumulative rainfall each year, and Fig. 8 shows the monthly rainfall each year. The daily and monthly rainfall data were calculated from the recorded hourly rainfall. The rainfall in the landslide area is characterized as having high seasonal and annual variation. In a given year, precipitation concentrates in the rainy season from June to September and with little to no precipitation during the dry season (see Figs. 7, 8). The cumulative rainfall in the rainy season was 715.5 mm, 689.5 mm, 636.5 mm, and 433.2 mm for 2013, 2014, 2015, and 2016, respectively. Rainstorm events with daily rainfall exceeding 50 mm are listed in Table 2, along with the corresponding rainfall characteristic parameters.

On an annual basis, different rainfall patterns exist. As shown in Fig. 7 and Table 2, the rainfall pattern in 2013 can be characterized as high frequency and high intensity. Five rainstorms occurred between June and July in 2013. The rainfall patterns are similar in 2014 and 2015 with two rainstorms occurred in June and August. In both years, a majority of rainfall events are of high frequency and low intensity, and the same level of monthly rainfall occurred in most months, especially in June and July (Fig. 8). The rainfall pattern in 2016 can also be characterized with high frequency and low intensity during the whole year, with a majority of daily rainfall lower than 25 mm (Fig. 7); however, the frequent rainfall during the rainy season led to a considerable monthly rainfall in June, July, and September (Fig. 8). During these four years, the maximum hourly and daily rainfall was 84.5 mm and 130 mm, respectively, both occurring on August 8–9 of 2014, whereas the maximum cumulative rainfall (R_{cum}) in a single rainfall event was 212 mm on August 16–19 of 2015.

Table 1 Type, installation, and operating condition of sensors in the Kualiangzi landslide from date of installation to December of 2016

Monitoring points	Monitoring parameter	Location	Depth of sensor (m)	Date of installation (yy/m/d)	Sampling interval	Period of record (up to 2016)
Y01	A	U		2011/4/1	Hourly	2011/4–2012/9
Y02	A	U		2013/5/27	Hourly	2013/6–2014/9, 2015/6–2016/11
PW01	B	U	49	2013/6/1	Hourly	2013/6–2013/12
PW02	B	M	40	2013/6/3	Hourly	2013/6–2015/6
PW1-1-1	B	M	35	2013/5/27	Hourly	2013/6–2015/6
PW1-1-2	B	M	34	2013/5/27	Hourly	2013/6–2013/12
PW1-2-1	B	L	16.8	2013/5/30	Hourly	2013/6–2015/6
PW1-2-2	B	L	21	2013/5/30	Hourly	2013/6–2013/12
PW1-3-1	B	L	16	2013/6/3	Hourly	2013/6–2013/12
PW1-3-2	B	L	15.5	2013/6/3	Hourly	2013/6–2015/6
PW1-4	B	L	18	2013/6/7	Hourly	2013/6–2013/12
UW1-3	C	L	22	2013/5/28	Hourly	2013/6–2016/12
UW1-4	C	L	12	2013/6/1	Hourly	2013/6–2016/12
UW1-5	C	L	18	2013/6/5	Hourly	2013/6–2016/12
GPS01	D	L		2012/9/6	Hourly	2012/9–2016/10
GPS02	D	L		2012/9/6	Hourly	2012/9–2016/10

A: rainfall; B: pore-water pressure; C: groundwater level; D: surficial displacement; U: the upper section of landslide; M: the middle section of landslide; L: the lower section of landslide

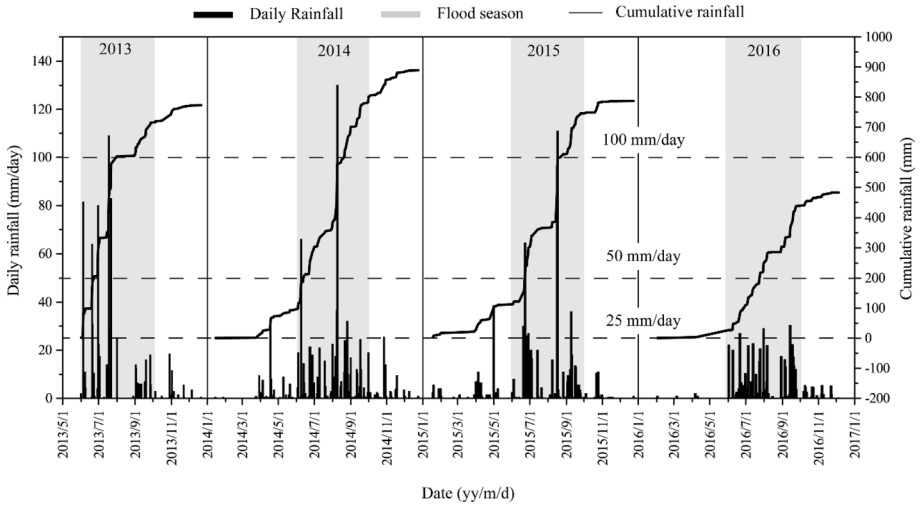

Fig. 7 Daily and cumulative rainfall at the Kualiangzi landslide from 2013 to 2016

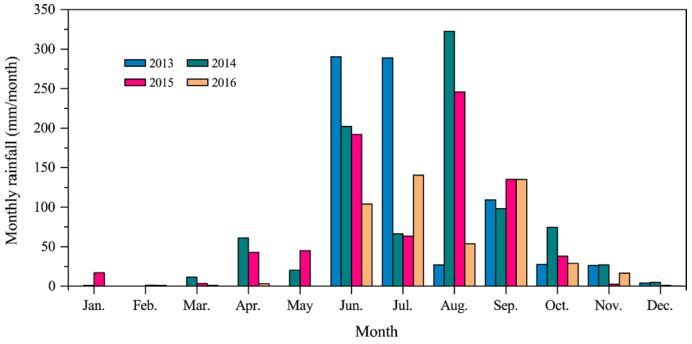

Fig. 8 Monthly rainfall of the Kualiangzi landslide from 2013 to 2016

3.2 Antecedent precipitation index

Many studies have reported the effect of antecedent precipitation index (*API*) on the groundwater response and the initiation of a landslide using different methods to calculate *API* (Kohler and Linsley 1951; Crozier and Eyles 1980; Crozier 1986; Glade et al. 2000; Matsuura et al. 2003; Ma et al. 2014; Chen et al. 2015). In the widely used expression developed by Crozier and Eyles (1980), *API* is regarded as the linear combination of daily rainfall in a period prior to a landslide event and on the day of the event and is widely adopted to determine the landslide-triggering rainfall threshold. Herein, our purpose is to study the relationship between API and groundwater response, which requires *API* at any time to be calculated in the groundwater response process, so the expression for API is re-written based on Padilla et al. (2014):

Table 2 Rainstorm events with daily rainfall exceeding 50 mm between 2013 and 2015 at the Kualiangzi landslide site

Year	Rainstorms	R_{cum}(mm)	I_{hmax}(mm/h)	I_{dmax}(mm/day)	T(h)	R_{ave}(mm/h)	API_{max} (mm/day)					
							3 days	7 days	10 days	15 days	30 days	60 days
2013	June 5	81.5	21	81.5	10	8.2	82.3	82.8	83.0	83.2	83.3	83.4
	June 20–21	95	16	64	13	7.3	85.0	110.8	125.0	140.9	163.1	183.9
	June 29–July 3	127	9	80	33	3.8	98.8	144.6	170.0	202.0	253.0	288.3
	July 18–20	142.5	24.5	109	41	3.5	126.2	170.3	201.9	246.7	329.1	268.4
	July 22	83	26	83	11	7.5	149.0	213.2	250.9	301.9	394.3	396.0
2014	June 9–10	67.5	24	66	8	8.4	73.4	83.5	89.0	97.8	119.2	142.3
	August 8–9	165.5	84.5	130	14	11.8	175.1	200.0	216.0	242.6	312.1	396.1
2015	June 23–24	87.5	17.5	64.5	23	3.8	86.5	104.0	110.8	120.0	143.0	188.2
	August 16–19	212	24.5	111	36	5.9	190.9	210.1	221.9	244.2	309.0	439.9

R_{cum}: cumulative rainfall; R_{ave} : average hourly rainfall; I_{hmax}: maximum hourly intensity; I_{dmax}: maximum daily intensity; T: actual rainfall duration; API_{max} maximum daily antecedent rainfall

$$\mathrm{API\_}T = P_t + \sum_{n=1}^{x} \left(\frac{1}{2}\right)^{\frac{n}{T}} P_t \tag{1}$$

where API_T is the antecedent precipitation index for a half-life of T (in days), and P_t is the precipitation at day t. The last term in Eq. (1) represents the antecedent precipitation decay within a period of x days staring from day t. If there are other rain events occurring on any day during the decay period of P_t, the amount of rain observed is added to the index (Kohler and Linsley 1951). The half-life T means that the precipitation P_t will be reduced to its half after T days, and its value reflects the decay velocity of precipitation. In this study, five half-lives: 3, 7, 15, 30, and 60 days were selected to calculate different API values. The results are plotted in Fig. 9 between June and December of each year. The maximum API values ($\mathrm{API_{max}}$) for different half-lives in each rainstorm are also summarized in Table 2. It is worth noting that, in this study, the API was regarded as a rainfall parameter which was just calculated from the monitored daily rainfall; hence, the influences of any other factors such as water level and landslide deformation were not considered in the API's calculation.

Figure 9 shows that the smaller the half-life, the steeper the API recession curve. For T=3 days, the occurrence of all peaks in API curve corresponded well with that of the daily rainfall. As T increases, the cumulative effect of antecedent rainfall becomes more significant, which could lead to the occurrence of maximum peak API lagging behind the maximum daily rainfall. For example, the maximum peak of API_60 was 23 and 10 days behind the maximum daily rainfall in 2014 and 2016, respectively. Referring to Eq. (1), the long lag time should be attributed to the long half-life in API calculation and the particular rainfall pattern in 2014 and 2016. In Figs. 9(b) and (d), it can be seen that there are many low- intensity rainfall events between June and December in both 2014 and 2016, including two rainstorms in 2014 (see Table 2). When the half-life was 60 days, each rainfall took longer time to decay to a low value. Finally, the precipitation accumulation from several rainfall events caused the later occurrence time of the maximum peak of API_60 relative to the maximum daily rainfall in 2014 and 2016. The relatively significant cumulative effect of antecedent rainfall in 2014 can be partly responsible for a slight landslide movement occurring on September 22 when the daily rainfall was only 24.5 mm (Fig. 9b). For 2013, the half-life did not significantly change the shape of API curve as the rainfall pattern was high frequency, long duration, and high intensity.

3.3 Relationship between rainfall and pore-water pressure

As shown in Fig. 6, nine piezometers were installed in different sections of the Kualiangzi landslide, most of which were close to the slip surface. Based on the available data (Table 1), Fig. 10 gives a general view of pore-water pressure response to hourly rainfall at different monitoring points, excluding PW01 and PW02, between June 2013 and June 2015. In this figure, pore-water pressure (PWP) is calculated from the sensor location. During the rainy season of 2013, the response of PWP to rainstorms was immediate in some monitoring points (e.g., PW1-1-1), but there was a noticeable lag in other monitoring points (e.g., PW1-3-2. A drastic drop of PWP occurred at five monitoring points (i.e., PW1-1-1, PW1-1-2, PW1-2-2, PW1-3-1, and PW1-3-2) during the rainstorm on July 22 and at PW1-4 on July 18–20, which can be attributed to the rainfall-induced landslide movement in the late rainy season of 2013 (Xu et al. 2016). Starting September 2013, the recorded PWP at PW1-1-1, PW1-1-2, PW1-2-1, PW1-2-2, and PW1-4 had mean values

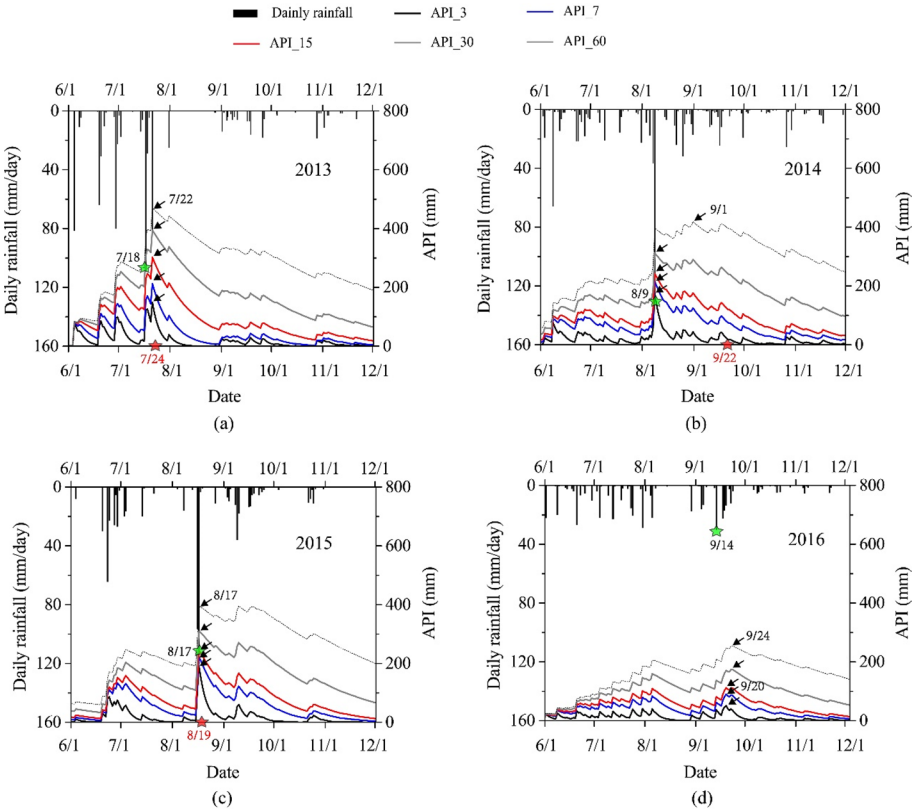

Fig. 9 Temporal variation in API for different half-lives and daily rainfall from 2013 to 2016. The green star symbol denotes the date (m/d) when the maximum daily rainfall occurred, while the black arrow denotes the date (m/d) when the maximum peak API occurred for different half-lives. The red star symbol denotes the date (m/d) when the maximum displacement rate occurred in the corresponding year

around 0 with minor fluctuations. In contrast, the recorded PWP at PW1-3-2 showed marked rise and fall during the rainy season of 2014, with values over 60 kPa during the whole recording period.

In order to better understand the relationship between rainfall and pore-water pressure, two rainfall parameters (i.e., daily rainfall and API) and two pressure parameters (i.e., PWP and PWPF) on a daily basis are simultaneously used for two monitoring points: PW1-1-1 and PW1-3-2, as shown in Fig. 11. PWPF is the pore-water pressure fluctuation and defined as the difference between the current and the previous PWP data. The rainfall duration under consideration is from June to November of 2013 and 2014, which contains a complete response process of pore-water pressure from significant rise during the rainy season and decay shortly after. Three half-lives of 3 days, 15 days, and 60 days were selected to represent the antecedent precipitation index with different decay velocities.

Figures 11a and c show the relationship between rainfall and PWP at PW1-1-1 and PW1-3-2, respectively, in 2013, and the following observations can be made. First, the peak PWPF was highly correlated to the maximum daily rainfall in a rainstorm, which was evident at PW1-3-2. Second, the recession curve of PW1-1-1 in a rainstorm was well

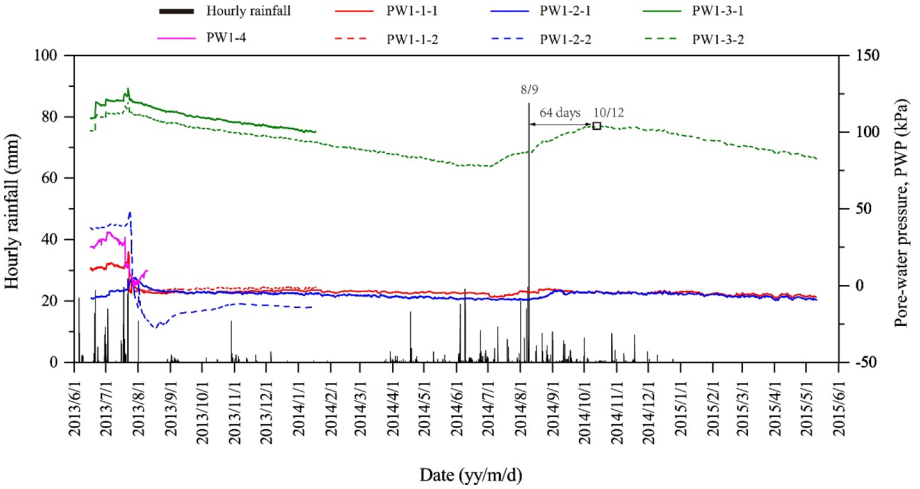

Fig. 10 A general view of PWP response to hourly rainfall from 2013 to 2015

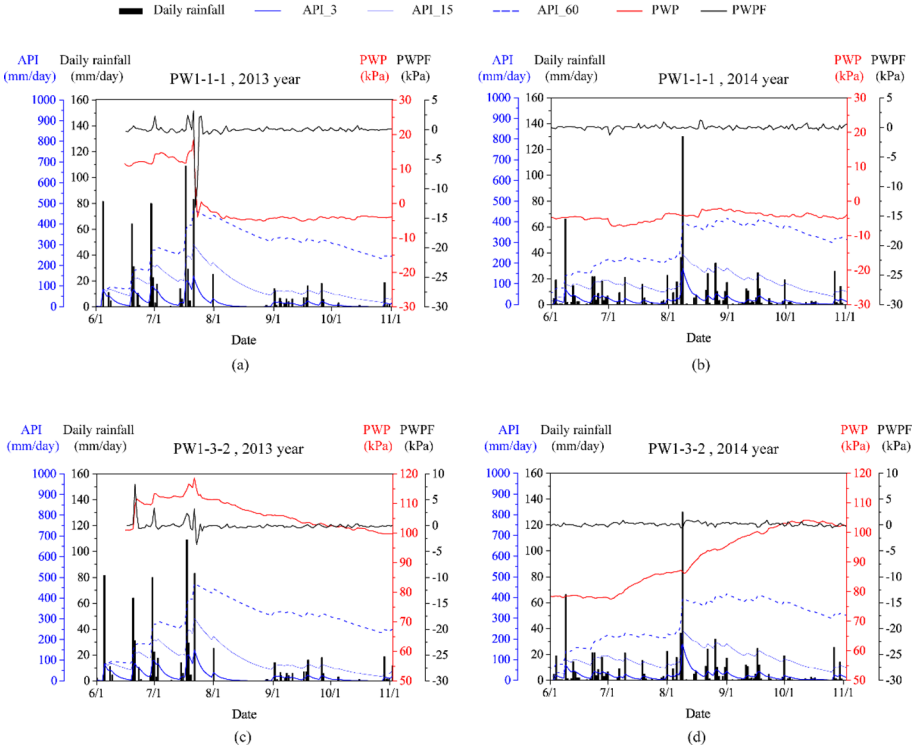

Fig. 11 Relationship between daily rainfall, API, PWP, and PWPF at select monitoring points during select period in 2013 and 2014

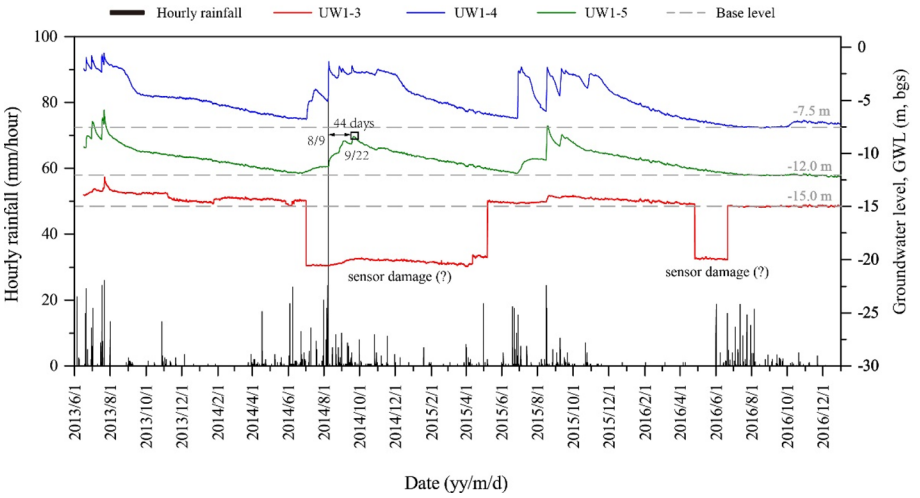

Fig. 12 A general view of GWL response to hourly rainfall from 2013 to 2016

correlated with the curve of API_60. Third, the rapid rise and fall of PWP over a short period at PW1-3-2 correlated well with API_3, whereas the slow decay correlated well with API_60; the rapid rise and fall of PWP corresponded to a rapid water recharge and drainage in the borehole PW1-3, suggesting a preferential flow in the slope.

Figures 11b and d show the corresponding plots in 2014. In contrast to the close correlation observed in 2013, the PWPF values at both monitoring points were smaller and unrelated to the daily rainfall in 2014. The PWP had a much weaker correlation with API. In this case, it is challenging to build a relationship between rainfall and pore-water pressure. Significant time lag was observed at PW1-3-2; this phenomenon might be associated with the distinctively different rainfall pattern of 2014, which was dominated by small, but frequent rainfall events with only two short-duration and high-intensity rainstorms. The first rainstorm on June 9–10 caused the first rise of PWP with a time lag of 26 days relative to the onset of rainstorm at PW1-3-2, whereas the second rainstorm on August 8–9 caused a peak PWP with a time lag of 64 days. Finally, the PWP response at PW1-3 was slower and longer with a smoother curve compared to the concentrated peaks in 2013. Another possible explanation is that the landslide movement in the rainy season of 2013 caused a big change of flow pathways, which increased the time required for water infiltration into the deeper zone and drainage out of the boreholes.

3.4 Relationship between rainfall and groundwater level

As shown in Fig. 6, three water-level gauges: UW1-3, UW1-4, and UW1-5 were installed in different sections of the Kualiangzi landslide to investigate the groundwater level (GWL) response. Figure 12 shows a general view of GWL responses to rainfall on an hourly basis between June 2013 and December 2016. Herein, GWL below ground surface (bgs) is defined as negative. A significant seasonal variation of GWL to rainfall from 2013 to 2015 was observed, with a large GWL fluctuation in the rainy season and a gradual recession to a base level in the dry season. The shape of the hydrograph depends on not only the rainfall characteristics but also the hydrological property of the aquifers; sometimes, it is also

related to the change of flow pathways caused by landslide movement. Compared to the rapid response to rainfall in the rainy season of 2013, UW1-5 cost a long time (44 days) to reach its peak GWL in the rainstorm on August 8–9 of 2014, which was also observed at PW1-3-2. Except for the relatively broad and smooth curve of UW1-5 in the rainy season of 2014 and the abnormal response possibly caused by the sensor malfunction at UW1-3 in the rainy season of 2014 and 2015, a fast-rising limb can be observed on the hydrographs of the three boreholes, suggesting a rapid GWL response to rainstorm in the rainy season. The peaks had very short duration, indicating the existence of rapid drainage pathways (i.e., preferential flow) in the slope. Comparing Fig. 10 and Fig. 12, UW1-3 exhibited a similar shape as PW1-1-1 and PW1-1-2 in the rainy season of 2013, both of which were installed in the middle section of the landslide consisting of extensive bedrock; UW1-5 also exhibited a similar shape as PW1-3-2 from 2013 to 2014, which was installed in the lower section with a thick covering soil. The GWL at UW1-4 in the lower section fluctuated somewhat differently from that at UW1-5, which might be attributed to local variations in stratigraphy.

Figure 13 shows the relationships among rainfall (daily rainfall and *API*), GWL, and ground water level fluctuation (GWLF) on a daily basis at UW1-3 and UW1-5, where GWLF is defined as the difference between the current and the previous GWL data. Two typical rainfall patterns in 2013 and 2015 were selected to represent the rainfall events. The soil–bedrock interface (i.e., 12 m bgs) was also denoted in the figure. It can be seen that GWL at UW1-3 fluctuated below the soil–bedrock interface (see Fig. 13a and b), whereas GWL at UW1-5 fluctuated above the interface (see Fig. 13c and d). Additionally, UW1-4 and UW1-5 recorded a base level in the dry season close to the interface during our observation period from 2013 to 2016 (see Fig. 12).

A time lag in GWL response relative to the onset of a rainstorm was observed, which correlates well with the rainfall pattern. During the rainy season with high-frequency and high-intensity rainfalls in 2013, GWL responded rapidly in the later period due to the increased saturation of rock/soil materials. For example, the time lag of peak GWL in the four successive rainstorms in 2013 was 3 days, 3 days, 1 day, and 0 day at UW1-5 (see Fig. 13c). The spatial and temporal differences in time lag of GWL response in 2013 were analyzed in detail by Xu et al. (2016); hence, this topic will not be discussed in further detail.

Similar to Figs. 11 and 13 also shows a close correlation between the peak GWLF and daily rainfall, GWL and API with a certain half-life. For example, UW1-5 was well correlated to API_15 in 2013. In the following, a correlation analysis was carried out based on the three-year monitoring data from 2013 to 2015 using three sets of characteristic parameters, namely peak GWLF and daily rainfall, peak GWLF and cumulative rainfall, and peak GWL and API with different half-lives.

Figure 14a and b shows the relationships between peak GWLF and two rainfall parameters (i.e., peak daily rainfall and cumulative rainfall of an event) at UW1-3, UW1-4, and UW1-5. Considering that both UW1-4 and UW1-5 responses were dominated by the similar aquifer system (i.e., porous aquifer system), their peak GWLFs were used together to carry out a correlation analysis, which results in a strong positive correlation with the rainfall parameters (Spearman's correlation coefficient $r > 0.8$). The correlation between peak GWLF and cumulative rainfall was higher than that between peak GWLF and peak daily rainfall, as indicated by the bigger correlation coefficient. The best fitting between peak GWLF and two rainfall parameters was an exponential relationship as shown in Fig. 14a and b. As the peak daily rainfall and cumulative rainfall increased, the peak GWLF increased first slowly and then rapidly. Compared to the significant fluctuation of

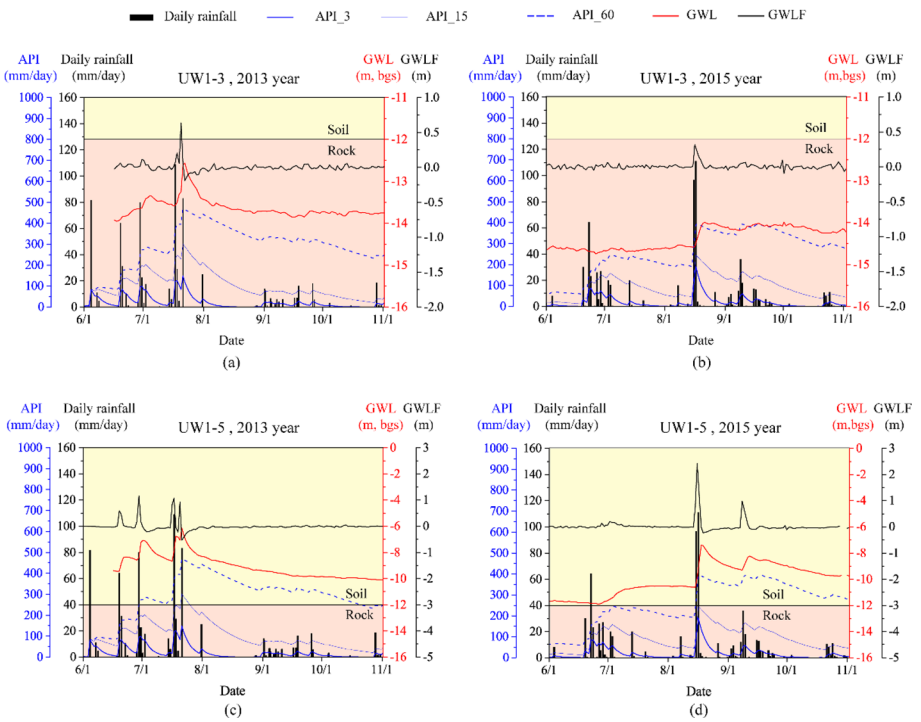

Fig. 13 Relationship between daily rainfall, API, GWL, and GWLF at select monitoring points during select period in 2013 and 2015

UW1-4 and UW1-5, the peak GWLFs at UW1-3, where the bedrock was extensively distributed, were very small (smaller than 0.8 m) and almost irrespective of rainfall intensity and cumulative rainfall.

Figure 14c and d shows the corresponding plots for peak GWL above sensor location (asl). It can be seen that the peak GWL was weakly correlated with peak daily rainfall and cumulative rainfall, with the correlation coefficient ($r=0.5$) much smaller than that between peak GWLF and rainfall parameters. Nevertheless, a curve fitting was still carried out between peak GWL and rainfall parameters, which results in a reverse exponential relationship. As the daily rainfall and cumulative rainfall increased, the peak GWL increased first and subsequently decreased. The peak GWLs at UW1-3 were smaller than those at the other two monitoring points during the same rainfall events. No curve fitting was carried out at UW1-3 due to the small number of data points.

Figure 15 shows the relationships between peak GWL and peak API with half-lives of 3, 7, 15, and 30 days in a rainfall event. In contrast, the peak GWL demonstrated a stronger correlation with peak API than that with rainfall parameters when the half-life was smaller than 30. The correlation coefficient between peak GWL and peak API_7 reached 0.8, and the best curve fitting between them was also an exponential relationship. Figure 15b indicates a fast rise of water level as API_7 increased up to 100 mm, followed by a plateaued response which was similarly observed in Padilla et al. (2014) after API reached a certain value, suggesting the porosity of rock/soil reached saturation with sufficient rainfall infiltration. At UW1-3, the correlation between peak GWL and peak API was uncertain due

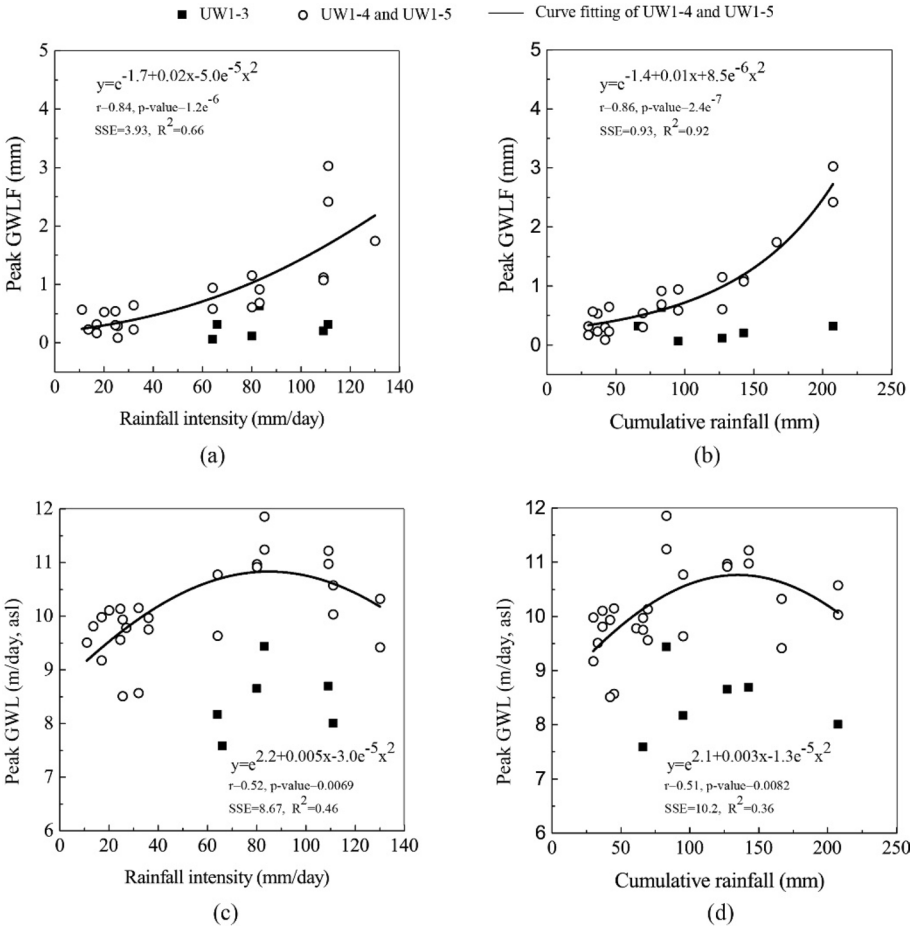

Fig. 14 Relationship between peak GWLF, peak GWL, and two rainfall characteristic parameters in an rainfall event over three-year period from 2013 to 2015: **a** peak GWLF vs. peak daily rainfall; **b** peak GWLF vs. cumulative rainfall; **c** peak GWL vs. peak daily rainfall; and **d** peak GWL vs. cumulative rainfall

to the limited data points. The large difference in the GWL response between UW1-3 and UW1-4/UW1-5 shown in Figs. 12, 13, 14 and 15 suggests potential topographic and stratigraphic effects on the GWL response, which will be discussed next.

3.5 Relationship between groundwater response and landslide movement

Figure 16a shows the monitored displacement of the Kualiangzi landslide from 2013 to 2015. According to Xu et al. (2016), the factor of safety for the slope was lower than 1.0 only in the rainy season of 2013. A rapid increase in the displacement rate from 2.5 mm/day on July 17 to 24.8 mm/day on July 24 and a large cumulative displacement of 87.3 mm were observed over this period. The rapid landslide displacement was accompanied by a drastic drop of PWP at five monitoring points (i.e., PW1-1-1, PW1-1-2, PW1-2-2, PW1-3-1, and PW1-3-2) during the rainstorm on July 22 and at PW1-4 on July 18–20 (see

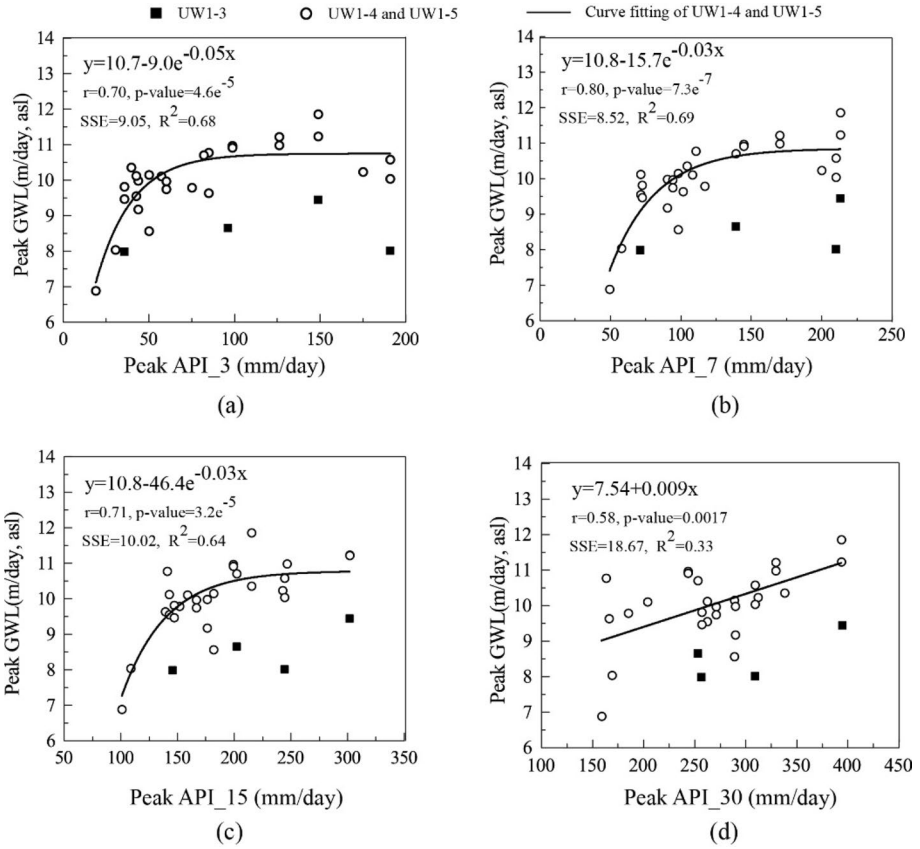

Fig. 15 Relationship between peak GWL and API with different half-lives in an rainfall event over three-year period from 2013 to 2015: **a** 3 days; **b** 7 days; **c** 15 days; and **d** 30 days

Fig. 10), suggesting an abrupt change of the flow pathways due to the large deformation in the deep zone. In the next two years, the maximum displacement rate was 2.7 mm/day and 3.4 mm/day in the rainy season of 2014 and 2015, respectively, although there were several rainstorms in both years with comparable rainfall intensity as that on July 18–20, 2013. The abnormally low displacement rate in 2014 and 2015 was accompanied by the subdued GWL response in the tension trough at the rear edge of the landslide (i.e., PW01) as shown in Fig. 16c–d.

For a hydraulically driven landslide in the nearly horizontal rock strata, the hydrostatic pressure in the tension trough plays a key role in initiating the movement (Zhang et al. 1994). Figure 16b–d shows a strong correlation between the slope movement and PWP at PW01 over three years from 2013 to 2015, although the recorded PWP values in the rainy season of 2014 and 2015 were much lower than those in 2013. Another observation from Fig. 16b–d is the relatively low correlation between the slope movement and PWP at PW1-3-2, UW1-4, and UW1-5 embedded in the sliding body, albeit high pressures were recorded in each rainy season. The lowest correlation was observed at UW1-4 where the sensor was embedded in the soil layer, about 4.0 m above the slip surface. Different degrees of correlation between slope displacement and PWP at different monitoring points

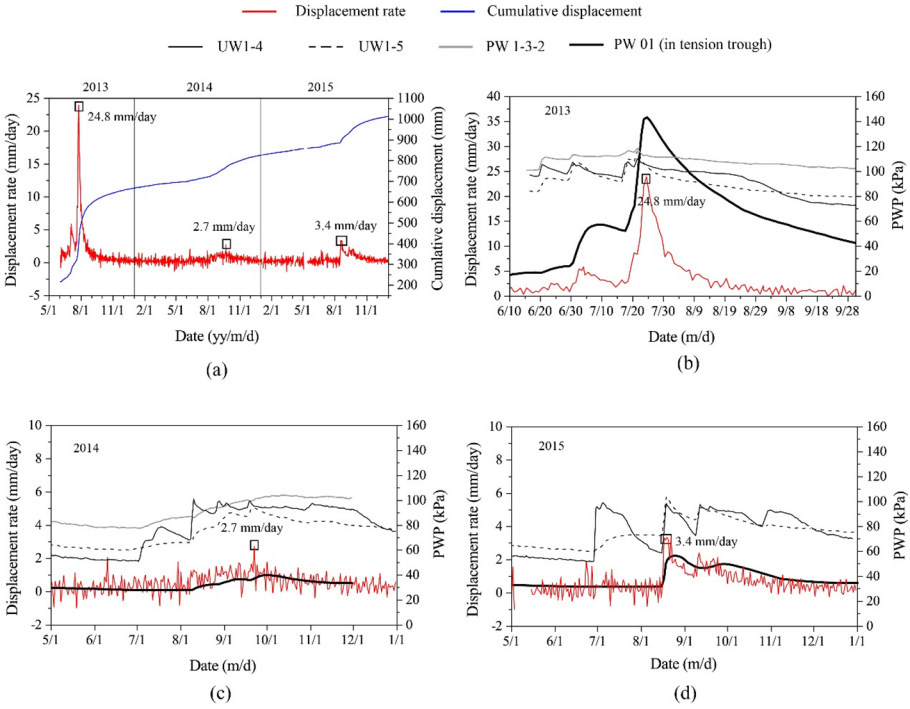

Fig. 16 Relationship between surficial landslide displacement and PWP in tension trough and sliding body: **a** displacement monitored over three years; **b** relationship in 2013; **c** relationship in 2014; and **d** relationship in 2015

suggest that PWP directly measured near the bottom slip surface is more useful when carrying out the real-time slope stability analysis on this type of landslide.

4 Discussions

Hydrograph analysis techniques have been well developed for hydrographs obtained from streams and springs (Moore 1992; Dewandel et al. 2003; Fiorillo 2014) and wells (Shevenell 1996; Kovács et al. 2015). It is widely accepted that the shape of the recession limb in a water-level hydrograph is largely dependent on the hydrological property of the aquifer, rather than rainfall characteristics. In a multi-aquifer system, the aquifer with high hydraulic conductivity can drain the recharged water much more quickly than the one with low hydraulic conductivity, resulting in segments with different slopes on the recession limb of the hydrograph. Hence, the shape of a complete recession curve can reflect the characteristics of the aquifer system. For example, Shevenell (1996) associated three segments with gradually deceasing slopes from the recession curves of hydrographs in a karst aquifer to three types of storage in the aquifer, namely conduit, fracture, and matrix.

A widely adopted equation to describe the recession process of water level in hydrogeology is as follows:

$$Q_t = Q_0 e^{-\lambda t} \tag{2}$$

where Q_t is the groundwater flow (discharge) at any time t, Q_0 is the initial flow, and λ is the recession coefficient depending only on the hydraulic property of the aquifer, which has the unit of [day^{-1}]. Moore (1992) linked the semi-log recession rates of streamflow with water levels in observation wells using the following equation:

$$\frac{\ln\left(Y_1/Y_2\right)}{\left(t_2 - t_1\right)} = \lambda = \frac{\ln\left(Q_1/Q_2\right)}{\left(t_2 - t_1\right)} \tag{3}$$

where Y_1 and Y_2 are water levels above installed sensor, and Q_1 and Q_2 are the associated flows corresponding to the water levels at time t_1 and t_2, respectively. Equation (3) indicates that the recession coefficient can be directly calculated from water-level time series in a well without requiring the amount of flow. This hydrograph analysis method is used in this study to estimate the recession coefficient of each recession segment.

As shown in the three well hydrographs in Fig. 12, a short interval between two successive rainstorms in a rainy season results in an incomplete recession of water level; in contrast, a long dry season results in a complete recession curve, which is more suitable for carrying out the hydrograph analysis. Figure 17 shows the complete hydrographs in a water year from June 2013 to June 2014. The recession curve of each hydrograph was first divided into several segments with different slopes in the semi-log plots. Three linear segments, named as Seg. 1, Seg. 2, and Seg. 3, were identified and used to approximate the recession process for both UW1-3 and UW1-5. Four linear segments, named as Seg. 1, Seg. 2a, Seg. 2b, and Seg. 3, were identified and used for UW1-4. Equation (3) was subsequently used to calculate the recession coefficient of each segment and the results are summarized in Table 3.

The different recession coefficients of these segments correspond to drainage through different geological units. To facilitate a comparison, the geological profile at each borehole is superimposed on the right side of each hydrograph in Fig. 17. The recession coefficient of Seg. 1 was one to two orders of magnitude larger than the coefficients of the other segments, corresponding to the relatively rapid flow through the highly permeable gravely soil at UW 1-4 and UW1-5, and well-developed vertical joints in the bedrock (see Fig. 4) at UW1-3. For each borehole, Seg. 3 had the lowest coefficient, corresponding to the slow and diffuse flow and long-term decline of water level in the dry season through the relatively less-permeable bedrock. Seg. 2 corresponds to the transition between the quick and slow flows in the aquifer system.

It is worth noting that a plateau segment appears on the hydrograph of UW1-4 after Seg. 1 (i.e., Seg. 2a in Fig. 17), which also appears annually in Fig. 12. The duration of the plateau varied from 2 days to several weeks. The plateau might be caused by the existence of relatively impermeable clayey soil underlying the gravelly soil. According to the stratigraphy in Fig. 6, lens-type clayey soil is located between the gravelly soil layer and bedrock layer, which is the thickest at UW1-4. The low hydraulic conductivity of the clayey soil significantly slowed down the drainage rate at UW1-4 when the water level fell below the upper boundary of the clay layer. Further investigation of the aquifer system and its effect on groundwater flow characteristics in the Kualiangzi landslide requires further verification through hydrological tests and is left for a future study.

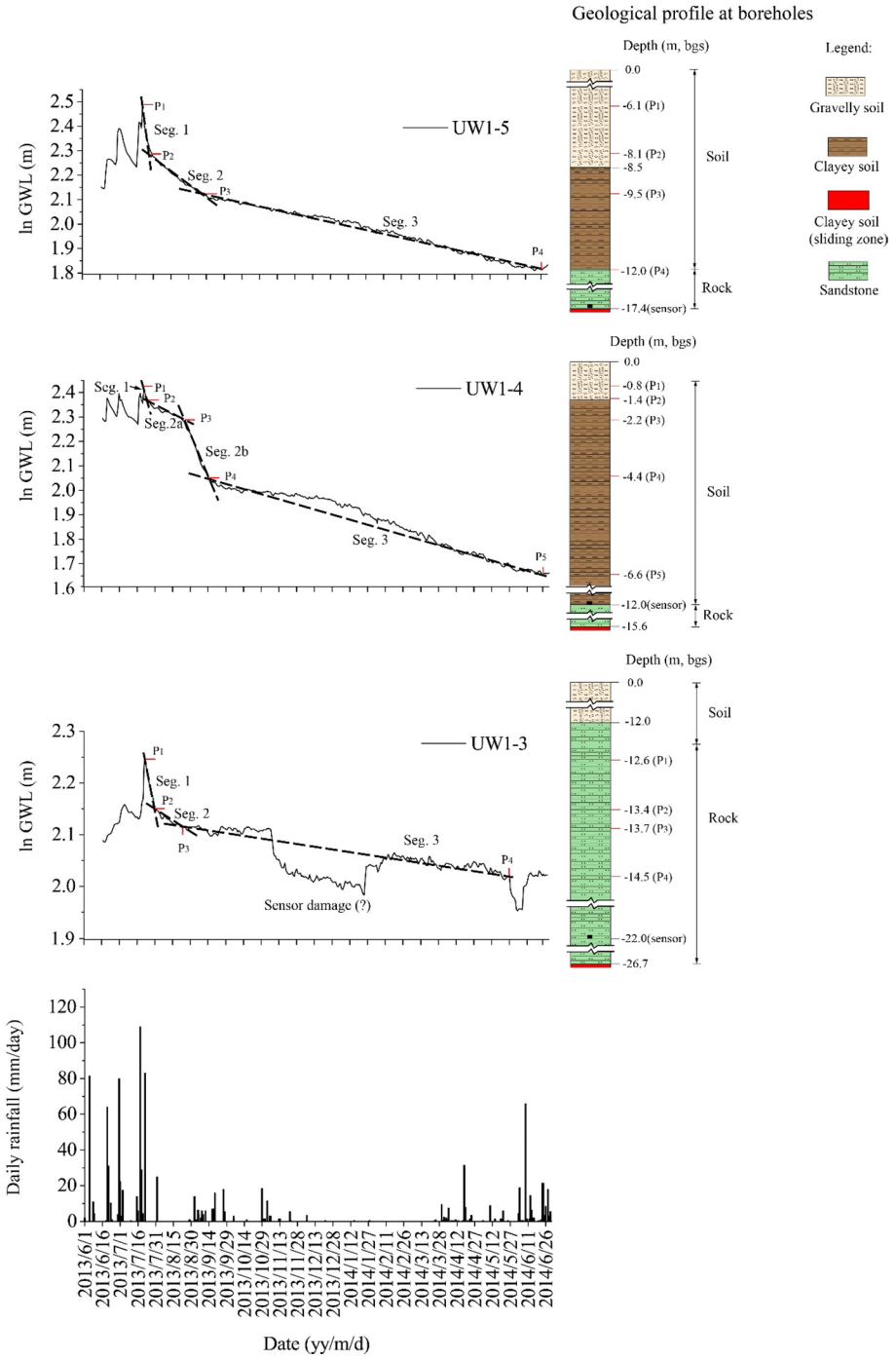

Fig. 17 Water-level hydrographs at UW1-3, UW1-4, and UW1-5 in a water year from June 2013 to June 2014

Table 3 Recession coefficients of different segments on water-level hydrographs

Monitoring point	Parameters (unit)	P_1	P_2	P_3	P_4	P_5	Seg. 1	Seg. 2		Seg. 3
								Seg. 2a	Seg. 2b	
UW1-3	t_n(day)	0	8	30	302					
	Y_n(m, asl)	9.44	8.60	8.29	7.49					
	λ_n(day^{-1})						1.15E−2	1.66E−3		3.74E−4
UW1-5	t_n(day)	0	7	47	338					
	Y_n(m, asl)	11.86	9.94	8.49	6.13					
	λ_n(day^{-1})						2.52E−2	3.94E−3		1.12E−3
UW1-4	t_n(day)	0	4	33	57	311				
	Y_n(m, asl)	11.24	10.64	9.83	7.65	5.39				
	λ_n(day^{-1})						1.36E−2	2.74E−3	1.05E−2	1.38E−3

5 Conclusions

In this study, the seasonal and annual variations of rainfall, groundwater, and surficial displacement of the Kualiangzi landslide were investigated, using the field measurements during a four-year period between 2013 and 2016. Much research effort has been directed to exploring the relationship between rainfall and groundwater response, based on different rainfall parameters and groundwater response parameters. The main conclusions can be drawn as a result of this study:

1. The rainfall patterns in the study area exhibited seasonal and annual variations. Precipitation concentrated in the rainy season from June to September of each year with little to no precipitation in the dry season. In 2013, the rainfall pattern was characterized as high frequency and high intensity, with a total of five rainstorms with daily precipitation exceeding 50 mm. In 2014 and 2015, the rainfall patterns were similar with two rainstorms of short duration and high intensity. In 2016, the rainfall pattern was characterized with low intensity, with a majority of daily rainfall smaller than 25 mm.
2. Both PWP and GWL responses in the landslide area were influenced by rainfall pattern, initial hydrological property of the underlying aquifer, and subsequent change of flow pathways caused by landslide movement, and could lag behind the onset of a rainstorm. The high-frequency rainstorms in 2013 caused concentrated peaks of PWP and GWL at UW1-4 and UW1-5, and PW1-3, where the groundwater responses were dominated by porous aquifer of high hydraulic conductivity. In contrast, a slower and prolonged response of PWP and GWL to rainfall in 2014 and 2015 was observed in most monitoring boreholes. The maximum time lag of peak groundwater response relative to the onset of the rainstorm on August 8–9 of 2014 was 64 days and 44 days for PWP at PW1-3-2 and GWL at UW1-5, respectively. In general, GWL exhibited a more rapid and pronounced response to rainfall than PWP under the same stratigraphy conditions.
3. In the lower section of the landslide, the peak GWL exhibited exponential relationships with cumulative rainfall and daily rainfall in a single rainfall event, with a stronger correlation for the former. The peak GWLF had a low correlation with the cumulative rainfall and daily rainfall, but exhibited an exponential relationship with API with a half-life of 7 days. In the middle section of the landslide, however, a relatively lower correlation between rainfall and groundwater response was observed.
4. Three types of groundwater flow were identified based on the recession coefficients of different segments of the water-level hydrographs in the landslide area. Seg. 1 with the largest recession coefficient corresponds to the relatively rapid flow through the highly permeable gravely soil (in UW 1-4 and UW1-5) and well-developed vertical joints in the bedrock (in UW1-3). Seg. 3 with the lowest recession coefficient corresponds to the slow and diffuse flow and long-term decline of water level in the dry season through the relatively less-permeable bedrock. Seg. 2 corresponds to the transition between the quick and slow flows in the aquifer system.

Acknowledgements This research is financially supported by the State Key Laboratory of Geohazard Prevention and Geoenvironment Protection Independent Research Project under Grant No. SKLGP2018Z015, and the Applied Basic Research Program of Sichuan Province under Grant No. 2021YFSY0036. The third author is a collaborator and supported by the US National Science Foundation under award No. CMMI-1453103.

Author contributions QX and JL performed the field monitoring; HL and TQ analyzed the data and wrote the manuscript.

Funding This research is financially supported by the State Key Laboratory of Geohazard Prevention and Geoenvironment Protection Independent Research Project under Grant No. SKLGP2018Z015, and the Applied Basic Research Program of Sichuan Province under Grant No. 2021YFSY0036. The third author is a collaborator and supported by the US National Science Foundation under Award No. CMMI-1453103.

Declarations

Conflict of interest There are no conflicts of interest to be declared.

References

Caine N (1980) The rainfall intensity-duration control of shallow landslides and debris flows. Geogr Ann Ser B 62(1–2):23–27

Chen CW, Saito H, Oguchi T (2015) Rainfall intensity–duration conditions for mass movements in Taiwan. progress in earth and planetary science. Progr Earth Planet Sci 2:14

Chen, SJ (2014) Study on shear strength properties of slip soils and deformation mechanism of Kualiangzi landslide in ZhongJiang of Sichuan. Dissertation of Master's Degree, Chengdu University of Technology. (in Chinese with English abstract)

Chigira M (2009) September 2005 rain-induced catastrophic rockslides on slopes affected by deep-seated gravitational deformations, Kyushu, southern Japan. Eng Geol 108(1–2):1–15

Crosta GB, Frattini P (2003) Distributed modelling of shallow landslides triggered by intense rainfall. Nat Hazards Earth Syst Sci 3(1/2):81–93

Crozier MJ (1986) Landslides: causes, consequences and environment. Croom Helm, London, p 35

Crozier MJ (1999) Prediction of rainfall-triggered landslides: a test of the antecedent water status model. Earth Surf Proc Land 24:825–833

Crozier, MJ, Eyles, RJ (1980) Assessing the probability of rapid mass movement. In: The New Zealand institution of engineers—proceedings of technical Groups (Ed.), Proc. Third Australia–New Zealand conference on geomechanics, Wellington, New Zealand, p. 2.47–2.51

Dewandel B, Lachassagne P, Bakalowicz M, Weng P, Al-Malki A (2003) Evaluation of aquifer thickness by analysing recession hydrographs. Application to the Oman ophiolite hard-rock aquifer. J Hydrol 274:248–269

Fiorillo F (2014) The recession of spring hydrographs, focused on karst aquifers. Water Resour Manag 28(7):1781–1805

Gabet EJ, Burbank DW, Putkonen JK, Pratt-Sitaula BA, Ojha T (2004) Rainfall thresholds for landslides in Himalayas of Nepal. Geomorphology 63(3/4):131–143

Glade T, Crozier M, Smith P (2000) Applying probability determination to refine landslide-triggering rainfall thresholds using an empirical '"antecedent daily rainfall model."' Pure Appl Geophys 157:1059–1079

Guzzetti F, Peruccacci S, Rossi M, Stark C (2008) The rainfall intensity-duration control of shallow landslides and debris flows: an update. Landslides 5(1):3–17

Hong YM, Wan S (2011) Forecasting groundwater level fluctuations for rainfall-induced landslide. Nat Hazards 57(2):167–184

Hong Y, Hiura H, Shino K, Sassa K, Suemine A, Fukuoka H, Wang GH (2005) Quantitative assessment of the in fluence of heavy rainfall on a crystalline schist landslide by monitoring system - a case study of the Zentoku landslide, Japan. Landslides 2:31–41

Huang SB, Cheng Q, Hu HT (2005) A study on distribution of Sichuan red beds and engineering environment characteristics. Highway 5:81–85 (**in Chinese with English abstract**)

Iverson RM (2000) Landslide triggering by rain infiltration. Water Resour Res 36(7):1897–1910

Iverson RM, Major JJ (1987) Rainfall, ground-water flow, and seasonal movement at Minor Creek landslide, Northweatern California: physical interpretation of empirical relations. Geol Soc Am Bull 99(4):579–594

Jakob M, Weatherly H (2003) A hydroclimatic threshold for landslide initiation on the north shore mountains of Vancouver, British Columbia. Geomorphology 54(3–4):137–156

Ji SW, Zhang ZY, Wang LY, Liu HC (2000) The mechanism of deformation and failure for the slope composed of nearly horizontal competent and incompetent intercalated rock mass strata. Chin J Geol Hazard Control 11(3):49–52 (**in Chinese with English abstract**)

Jitousono T, Shimokawa E, Teramoto Y (2008) Debris flow induced by deep-seated landslides at Minamata City, Kumamoto Prefecture, Japan in 2003. Int J Eros Control Eng 1(1):5–10

Kohler, MA, Linsley, RK (1951) Predicting the runoff from storm rainfall. U.S. Weather Bureau Research Paper 34 (Washington, DC)

Kovács A, Perrochet P, Darabos E, Lénárt L, Szűcs P (2015) Well hydrograph analysis for the characterisation of flow dynamics and conduit network geometry in a karst aquifer, Bükk mountains, Hungary. J Hydrol 530:484–499

Krkač M, Špoljarić D, Bernat S, Arbanas SM (2017) Method for prediction of landslide movements based on random forests. Landslides 14(3):947–960

Li WC, Dai FC, Wei YQ, Wang ML, Min H, Lee LM (2016) Implication of subsurface flow on rainfall-induced landslide: a case study. Landslides 13:1109–1123

Lv HB, Ling CP, Hu BX, Ran JX, Zheng YN, Xu Q, Tong JX (2019) Characterizing groundwater flow in a translational rock landslide of southwestern China. Bull Eng Geol Env 78:1989–2007

Ma TH, Li CJ, Lu ZM, Wang BX (2014) An effective antecedent precipitation model derived from the power-law relationship between landslide occurrence and rainfall level. Geomorphology 216:187–192

Matsuura S, Asano S, Okamoto T, Takeuchi Y (2003) Characteristics of the displacement of a landslide with shallow sliding surface in a heavy snow district of Japan. Eng Geol 69:15–35

Matsuura S, Asano S, Okamoto T (2008) Relationship between rain and/or meltwater, pore-water pressure and displacement of a reactivated landslide. Eng Geol 101:49–59

Moore GK (1992) Hydrograph analysis in a fractured rock terrane. Ground Water 30(3):390–395

Ogawa S, Ikeda T, Kamei T, Wada T (1987) Field investigations on seasonal variations in the groundwater level and pore water pressure in landslide areas. Soils Found 27(1):50–60

Padilla C, Onda Y, Iida T, Takahashi S, Uchida T (2014) Characterization of the groundwater response to rainfall on a hillslope with fractured bedrock by creep deformation and its implication for the generation of deep-seated landslides on Mt. Wanitsuka, Kyushu Island. Geomorphology 204:444–458

Postance B, Hillier J, Dijkstra T, Dixon N (2018) Comparing threshold definition techniques for rainfall-induced landslides: a national assessment using radar rainfall. Earth Surf Proc Land 43:553–560

Prokešová R, Medveďová A, Tábořík P, Snopková Z (2013) Towards hydrological triggering mechanisms of large deep-seated landslides. Landslides 10:239–254

Ran QH, Hong YY, Li W, Gao JH (2018) A modelling study of rainfall-induced shallow landslide mechanisms under different rainfall characteristics. J Hydrol 563:790–801

Ruette JV, Papritz A, Lehmann P, Rickli C, Or D (2011) Spatial statistical modeling of shallow landslides-validating predictions for different landslide inventories and rainfall events. Geomorphology 133:11–22

Saito H, Nakayama D, Matsuyama H (2010) Two types of rainfall conditions associated with shallow landslide initiation in Japan as revealed by normalized soil water index. Sci Online Lett Atmos, SOLA 6:57–60

Sangrey DA, Harrop-Williams KO, Klaiber JA (1984) Predicting ground-water response to precipitation. J Geotech Eng 110(7):957–975

Shevenell LA (1996) Analysis of well hydrographs in a karst aquifer: estimates of specific yields and continuum transmissivities. J Hydrol 174(3–4):331–355

Tsou CY, Feng ZY, Chigira M (2011) Catastrophic landslide induced by Typhoon Morakot, Shiaolin, Taiwan. Geomorphology 127(3–4):166–178

Uchida T, Asano Y, Ohte N, Mizuyama T (2003) Seepage area and rate of bed rock groundwater discharge at a granitic unchanneled hillslope. Water Resour Res 39:1–12

Vallet A, Charlier JB, Fabbri O, Bertrand C, Carry N, Mudry J (2016) Functioning and precipitation-displacement modelling of rainfall-induced deep-seated landslides subject to creep deformation. Landslides 13:653–670

Van Asch ThWJ, Buma JT (1997) Modelling groundwater fluctuations and the frequency of movement of a landslide in the Terres Noires region of Barcelonnette (France). Earth Surf Proc Land 22:131–141

Van Asch ThWJ, Hendriks MR, Hessel R, Rappange FE (1996) Hydrological triggering conditions of landslides in varved clays in the French Alps. Eng Geol 42:239–251

Wei ZL, Lü Q, Sun HY, Shang YQ (2019) Estimating the rainfall threshold of a deep-seated landslide by integrating models for predicting the groundwater level and stability analysis of the slope. Eng Geol 253:14–26

Xu Q, Liu HX, Ran JX, Li WH, Sun X (2016) Field monitoring of groundwater responses to heavy rainfalls and the early warning of the Kualiangzi landslide in Sichuan Basin, southwestern China. Landslides 13(6):1–16

Zhang ZY, Wang ST, Wang LS (1994) The analytical principle in engineering geology. Beijing Geological Publishing House, Beijing

Zhang WJ, Chen YM, Zhan LT (2006) Loading/Unloading response ratio theory applied in predicting deep-seated landslides triggering. Eng Geol 82:234–240

Authors and Affiliations

Han-Xiang Liu[1,2] · Qiang Xu[1,2] · Tong Qiu[3] · Jiang Li[1]

✉ Han-Xiang Liu
hxliu_86@163.com

[1] College of Engineering and Civil Engineering, Chengdu University of Technology, Chengdu, China

[2] State Key Laboratory of Geohazard Prevention and Geoenvironment Protection, Chengdu University of Technology, Chengdu, China

[3] Department of Civil and Environmental Engineering, Pennsylvania State University, University Park, USA